Accurate band alignment at the amorphous Al_2O_3/p-Ge(100) interface determined by hard x-ray photoelectron spectroscopy and density functional theory

Nicholas F. Quackenbush,[1,*] Eric Cockayne,[1] James M. Ablett,[2] D. Peter Siddons,[3] Joseph C. Woicik,[1] and Abdul K. Rumaiz[3,†]

[1]*National Institute of Standards and Technology, Gaithersburg, Maryland 20899, USA*
[2]*Synchrotron SOLEIL, L'Orme des Merisiers, Boîte Postale 48, St Aubin, 91192 Gif-sur-Yvette, France*
[3]*National Synchrotron Light Source-II, Brookhaven National Laboratory, Upton, New York 11973, USA*

(Received 31 August 2018; published 30 November 2018)

We have investigated the band alignment at the interface of amorphous aluminum oxide (am-Al_2O_3) grown by atomic layer deposition on p-Ge(100) and the effects of postgrowth annealing using hard x-ray photoelectron spectroscopy and density function theory (DFT). Accurate determination of the valence-band offsets was obtained by comparing the experimentally measured valence bands with DFT-calculated densities of states. The am-Al_2O_3 density of states calculated from a weighted ensemble of crystalline Al_2O_3 structures gives excellent agreement with experiment, sufficiently capturing the nonlinear shape of the valence-band edge. We report a valence-band offset of 2.60 ± 0.1 eV for am-Al_2O_3/p-Ge, which is reduced by 0.20 eV upon annealing as interfacial GeO_x is formed.

DOI: 10.1103/PhysRevMaterials.2.114605

The exact energy-band alignments at semiconductor heterojunctions are critical to the design and performance of even the simplest semiconductor devices [1–3]. Energy barriers and spatial distributions of charge carriers at an interface are directly dependent on these quantities, thus providing a scheme for device properties to be appropriately tailored. It is therefore of great importance to measure band offsets with the highest possible degree of accuracy for any heterojunction of technological interest [4–6]. One such heterojunction that is gaining importance is the interface between amorphous Al_2O_3 (am-Al_2O_3) and germanium [7–11]. The exceedingly high hole mobility offered by germanium makes it an attractive alternative to silicon as a channel material for many high-mobility devices [12,13]. However, there are several challenges in developing germanium wafer process flows, due to the low thermal stability and water solubility of its native oxide. Substituting the oxide for am-Al_2O_3 has the advantages of high thermal and chemical stability coupled with low electrical conductivity and low cost of fabrication. Furthermore, deposition of am-Al_2O_3 on clean germanium surfaces can produce atomically abrupt interfaces allowing for reliable determination of interface properties including band offsets [9].

While this particular heterojunction is relevant for a wide range of electronic devices, the current work is motivated by the potential use of am-Al_2O_3 as a low-κ oxide for Ge-based sensing applications. Ge has been the material of choice in detectors of high-energy x rays and gamma rays for many years, largely because it is relatively easy to obtain high-quality material in large quantities. Current monolithic Ge-based radiation detectors rely on trenches for pixel isolation [14,15]. The development of robust oxide-based Ge-wafer processing would enable more interesting devices for radiation sensing, such as drift detectors or charge-coupled devices (CCDs). Much of the progress in Ge technology in general has been driven by the success of high-κ materials grown on Ge. The higher dielectric constant clearly offers advantages for device scaling, as demonstrated by the realization of the submicron Ge transistor [16] using HfO_2 as the gate oxide; however, this is not the case for sensing applications. The resolution of detectors, which is usually measured in terms of equivalent noise charge (ENC) depends on the total capacitance of the system, making low-κ oxides desirable for sensing applications [17]. Along with stability and density of defects, a clear understanding of the energy-band alignments is critical in assessing an oxide for a given semiconductor.

Here, we go a step further than previous works by combining high-resolution hard x-ray photoelectron spectroscopy (HAXPES) measurements and density functional theory (DFT) calculations to determine the valence-band offset at the am-Al_2O_3/p-Ge interface. The am-Al_2O_3 density of states (DOS) predicted from a simple weighted average of DFT DOS results for an ensemble of crystalline Al_2O_3 is used to more accurately locate the top of its valence band. Additionally, taking advantage of the larger information depth offered by HAXPES, we also study the effect of annealing on the electrical properties of this interface at a technologically relevant thickness.

Thin 20 Å am-Al_2O_3 films were grown on high-purity p-type Ge(100) substrates by thermal atomic layer deposition (ALD) [18]. The Ge substrates were first dipped in dilute H_2O_2 and thoroughly rinsed in deionized water to remove the native oxide. The deposition was performed via a reaction sequence consisting of half reactions of the Al precursor trimethylaluminium and an oxidation reaction using water.

*nicholas.quackenbush@nist.gov
†Author to whom correspondence should be addressed: rumaiz@bnl.gov

This was done at a temperature of 200 °C, yielding a deposition rate of ∼1 Å/loop. Postgrowth annealing was performed at various temperatures in a nitrogen environment. Metal-oxide semiconductor (MOS) capacitors were fabricated after the annealing step by photolithography using aluminum top gates. Capacitance-voltage (C-V) measurements were performed using a custom probe station equipped with a precision semiconductor parameter analyzer.

DFT calculations were performed using the VASP (Vienna *Ab initio* Simulation Package) software program [19]. The Perdew-Burke-Ernzerhof (PBEsol) generalized gradient approximation (GGA) was used for the exchange-correlation functional [20]. Projector augmented wave pseudopotentials [21,22] were used. All relaxations were performed with a plane-wave cutoff energy of 500 eV and a Γ centered k-point grid whose mesh in each Cartesian dimension was the nearest integer to 24 Å divided by the corresponding lattice parameter.

HAXPES was performed with 7 keV excitation energy using the high-resolution Si(333) reflection from a Si(111) double-crystal monochromator at the GALAXIES beam line at SOLEIL [23,24]. The hemispherical photoelectron analyzer was set to 200 eV pass energy resulting in an overall experimental resolution of ∼300 meV as determined from fitting a Fermi distribution function to the top of the valence band of a reference gold foil. All energies are calibrated using the Fermi level (E_F) and Au 4f core lines of the gold foil reference in electrical contact with the sample. The x rays were 10° glancing incidence on the sample surface and the cone of the photoelectron analyzer was oriented parallel to the polarization vector of the incident x-ray beam.

The valance-band offset at a given heterojunction (HJ) can be measured with high precision by photoemission via Kraut's method, in which the valence energy separation (ΔE_V) is determined by referencing the core-level energies in the heterojunction to that of the respective stand-alone materials or sufficiently thick films [4]. For the case of Al_2O_3/Ge, the valence-band offset is determined by

$$\Delta E_V = (E_{\mathrm{Al}1s} - E_V)_{\mathrm{Al_2O_3}} - (E_{\mathrm{Ge}3d} - E_V)_{\mathrm{Ge}} - (E_{\mathrm{Al}1s} - E_{\mathrm{Ge}3d})_{\mathrm{HJ}}, \quad (1)$$

where all energies are referenced to E_F. The largest uncertainty of this method lies in the precise determination of the valence-band maxima of each reference material, owing to the inherently nonsymmetric line shape, which is further convoluted by instrumental resolution, in contrast to the often sharp, well-defined peaks of core levels. The highest accuracy is therefore obtained by comparing the theoretical DOS calculated by first principles to the measured valence band, after applying a Gaussian convolution function to account for the instrumental broadening [6,25]. This method gives the correct line shape to fit to the experiment, while the DFT can be used to unambiguously determine where the unbroadened DOS goes to zero. This combined experimental-theoretical method provides much better precision than is afforded by experimental extrapolation alone, and is often within ±0.1 eV.

To obtain the highest accuracy in this case, it is especially important to appropriately model and predict the valence-band DOS of the amorphous material. There are many known crystalline polymorphs of Al_2O_3 comprised from Al ions both

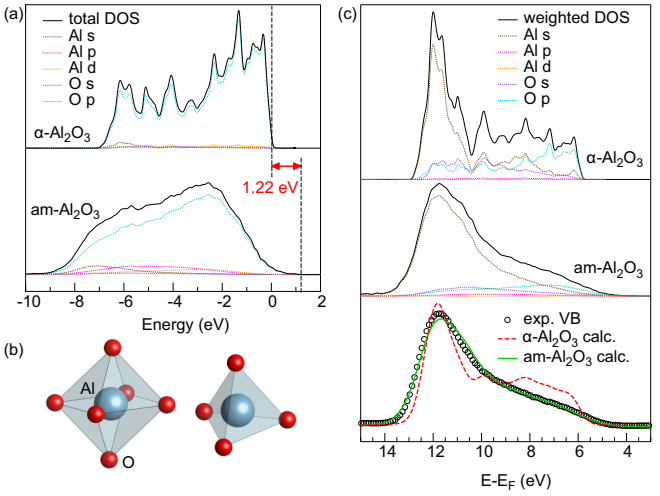

FIG. 1. (a) Calculated total and partial densities of states for crystalline (α-) and amorphous (am-) Al_2O_3. (b) Common Al-O coordinations found in Al_2O_3 polymorphs: octahedron (left) and tetrahedron (right). (c) Cross-section weighted total and partial densities of states for α- and am-Al_2O_3, including a direct comparison of each to the HAXPES valence-band spectrum after broadening (bottom).

octahedrally and tetrahedrally coordinated with oxygen [as depicted in Fig. 1(b)] [26]. In an amorphous oxide, despite the lack of long-range order in their packing, these local motifs are generally well preserved due to the high electronegativity of the oxygen anions [27,28]. Thus the general structural effect of amorphization is the variation of the metal-oxygen-metal angles and associated chemical bonding, while the first coordination shell bonding is largely unperturbed [29]. However, in am-Al_2O_3, the relative amounts of these different Al environments may also be significantly different from the crystalline phases.

Past density-functional-theory (DFT) studies of the electronic structure of am-Al_2O_3 have used the melt-quench algorithm to create periodic models for am-Al_2O_3 with order of 100 atoms per unit cell [30–32]. While these models provide useful insight into the local atomic and electronic structures of am-Al_2O_3, the number of distinct Al environments is limited by the size of the cell. Because of the N^3 scaling of plane-wave DFT calculations, it becomes computationally prohibitive to investigate significantly larger supercells.

In this work, we instead investigate the electronic structure of am-Al_2O_3 by creating an ensemble of metastable periodic Al_2O_3 structures and averaging their electronic structures. A similar approach was recently used by Nahas *et al.* [33]. We hypothesize that the electronic DOS in am-Al_2O_3 is driven mainly by the local environment seen by the Al and O atoms. By creating an ensemble of periodic structures with small to medium unit-cell sizes, we aim to mimic the large number of distinct local environments of a large unit-cell model, with less computational cost. Our hypothesis is justified *a posteriori* by the good agreement with experiment.

To generate the ensemble of periodic Al_2O_3 structures, we used the random-structure generation, mutation, and "mating" tools of the GASP genetic algorithm software [34,35]. The

Al_2O_3 structures were limited to 60 atoms per cell. In a run that generated 800 test structures, 139 distinct metastable Al_2O_3 structures were obtained after eliminating duplicates and structures where O_2 molecules formed (see Supplemental Material [36]). The ensemble of structures contained over 1500 Al and 2250 O positions. The DOS of each structure was calculated under DFT-GGA. The individual DOS were then each weighted with a Boltzmann factor $\exp(-E_{\text{atom}}/T_{\text{melt}})$, where E_{atom} is the binding energy per atom of the structure and T_{melt} is the melting temperature of corundum Al_2O_3. Finally, the weighted DOS were averaged to model the DOS for am-Al_2O_3.

Figure 1(a) shows the resulting total and partial densities of states of the Boltzmann-averaged amorphous phase as compared to the highly stable corundum phase α-Al_2O_3, aligned such that zero energy represents the topmost occupied state of α-Al_2O_3. The am-Al_2O_3 valence-band DOS looks similar to that of the α-Al_2O_3 phase albeit with broadened features, and closely resembles that of previous calculations using the melt-quench approach [30]. Here, we also determine that as compared to its crystalline counterpart, the band tailing due to amorphization effectively raises the valence-band maximum energy by 1.22 eV. Finally, we note that the am-Al_2O_3 valence DOS becomes less dominated by O $2p$ states due to increased orbital mixing possibly arising from the structural disorder. These overall trends are consistent with observations in other disordered oxide and nitride materials [27–29,37,38].

The high information depth of HAXPES is advantageous for probing buried interfaces; however, photoionization cross-section effects can become more pronounced at high excitation energies. To appropriately compare the DFT-predicted DOS with experiment, the calculated partial densities of states must be weighted by their respective photoionization cross section (σ) for the excitation energy used in the experiment. Figure 1(c) shows the DOS of each phase after weighting by the relativistic photoionization cross sections for 7 keV photons [39]. Each cross section was normalized by the orbital degeneracy $(2j+1)$, due to their incomplete shells, to achieve a per-electron basis [40]. The Al $3d$ cross section was assumed to be negligible ($\sigma_{\text{Al}\,3d} \approx 0$), as it is expected to be orders of magnitude below the Al $3s$ and $3p$ cross sections. The resulting weighted DOS of each phase appear starkly different to the actual DOS. The predominant O $2p$ partial DOS becomes overshadowed by the Al $3s$ states as a result of the ratio of their cross sections, $\sigma_{\text{Al}3s}/\sigma_{\text{O}2p} \sim 84$.

After broadening each weighted DOS with a Gaussian line shape to match the experimental resolution, the theoretical valence bands are compared to the valence-band HAXPES spectrum of a thick (700 Å) am-Al_2O_3 film. The predicted am-Al_2O_3 valence band gives exceptional agreement with experiment, while the crystalline phase does not. This confirms both the amorphous nature of the ALD-grown film and our genetic algorithm-based theoretical approach.

Looking now to the topmost valence states, Fig. 2 shows an expanded view of the top of the measured valence band of the thick am-Al_2O_3 reference film, as well as a bare p-Ge(100) surface, each overlaid with the calculated valence band (cross-section weighted and broadened DFT), which are aligned to give the best fit to the leading edge of the experimental spectra. This is because GGA-DFT does not necessarily give an accurate scaling of the binding energy axis, and therefore the error will increase with increasing binding energy, and the relevant number is the cutoff of states at zero energy or the valence-band maximum.

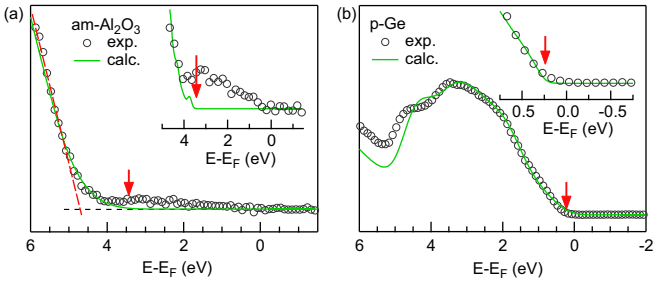

FIG. 2. (a) The top of the am-Al_2O_3 valence band compared to the DFT calculated valence band. (b) The top of the Ge valence band compared to theory. The insets show a zoomed-in region of the HAXPES spectra compared to the unbroadened cross-section-weighted DFT.

The top of the valence band is defined here in each material where the *unbroadened* DOS goes to zero, shown in the insets of Fig. 2. For am-Al_2O_3 the HAXPES shows a low density of occupied states within the gap. These in-gap states could be due to oxygen vacancies or other defects, which were not included in our calculations [41]. Another possible origin, deriving from the amorphous structure and different available coordinations of the Al ions, is local *undercoordination* of certain oxygen anions as observed in the prototypical amorphous oxide semiconductor indium gallium zinc oxide (IGZO) [42–44]. Regardless of their origin, here we assume they are not intrinsic to am-Al_2O_3. Indeed, they are not present in the predicted DOS, which reveals the intrinsic valence-band maximum at 3.45 eV.

It has become somewhat common practice to extrapolate a line tangent to the top of the valence-band spectrum to zero to define the valence-band maximum. Such an approach for an amorphous oxide material may introduce significant error, owing to the highly nonlinear valence-band edge. In the case of am-Al_2O_3, this method results in a valence-band maximum (VBM) that is 1.3 ± 0.2 eV higher in binding energy than when the theoretical line shape is explicitly considered, where the error largely arises from the choice of the bounds for the linear fit. We also note that this value can be significantly affected by the dramatic photoionization cross-section effects [25].

Determination of the VBM energy is more straightforward for crystalline germanium. Explicitly considering the theoretical line shape and the straight-line approximation results in VBM values that agree within the error. The predicted DOS gives an excellent fit in the top of the valence-band region. The Ge valence-band maximum is determined to be 0.24 eV, consistent with its bulk p-type doping.

In the core-level regions of the as-deposited am-Al_2O_3/Ge heterojunction, we observe no additional features due to chemical effects with respect to the reference materials. Most notably, there is no evidence of Ge surface oxidation during deposition (discussed further below). Additionally, no broadening of these core lines within the experimental resolution

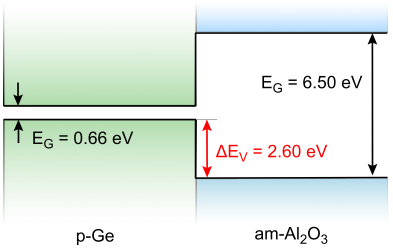

FIG. 3. Schematic energy-band alignment of the am-Al_2O_3/p-Ge heterojunction showing the measured valence-band offset ΔE_V of 2.60 eV.

is observed in either material, indicating that the bands are essentially flat within our probing depth, and thus no additional band-bending effects need to be considered [45]. The core-level energies in the heterojunctions were determined by fitting a single Voigt peak for Al 1*s*, and two Voigt peaks for the spin-orbit split Ge 3*d* doublet (taking the centroid value of the Ge $3d_{5/2}$), after subtracting a Shirley-type background. These values, combined with the valence-band maxima, reveal a valence-band offset of 2.60 ± 0.1 eV via Eq. (1).

This valence-band offset energy is markedly different from previous reports, where only linear extrapolation methods have been applied [7–11]. Taking into account the band tailing of the amorphous material makes clear that the linear extrapolation method overestimates the valence-band offset in this heterojunction by over 1 eV. Furthermore, the full band alignment construction is altered since the conduction-band offset is simply deduced from the valence-band offset along with independent band-gap values. A similar discrepancy of ∼1 eV has been observed for the related am-Al_2O_3/GaAs heterojunction, where the valence-band offset measured by photoemission is in disagreement with complementary internal photoemission measurements [46]. This could be explained by the failure of the linear extrapolation method used to find the valence-band maximum in the photoemission measurements of am-Al_2O_3 in previous works.

The schematic band alignment at the am-Al_2O_3/p-Ge interface as determined in this work is shown in Fig. 3. Considering a band gap of 0.66 eV for Ge and the significantly larger gap of Al_2O_3, this confirms a type-I straddling band-gap alignment for this interface, i.e., both the valence- and conduction-band energies of Ge lie within the gap of am-Al_2O_3. Here we have used a band gap of 6.50 eV for am-Al_2O_3 resulting in a conduction-band offset of 3.24 eV [9,10]. We note that reported band-gap values can range from 6.2 to 6.9 eV based on growth conditions and measurement technique, while the amorphous band gap is consistently lower than the crystalline gap in both theory and experiment, confirming that the band gap is indeed sensitive to the amorphous band tailing we observe here [31,47,48].

The effects of thermal annealing on the properties of this interface were also investigated. The am-Al_2O_3/p-Ge films were each annealed for 1 hour at various temperatures up to 500 °C. The corresponding Ge 3*d* and Al 1*s* core levels are shown in Fig. 4 referenced to the Al 1*s* energy to highlight their relative energy separation. After annealing to 200 °C and 300 °C, both core levels are indistinguishable from the

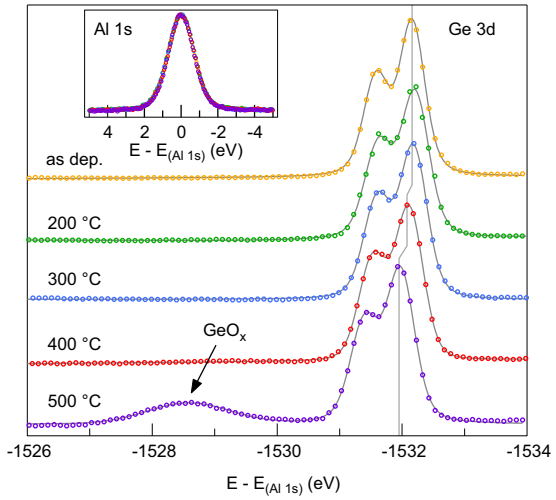

FIG. 4. Ge 3*d* core-level HAXPES spectra from am-Al_2O_3/Ge after annealing. The data have been aligned to the Al 1*s* core line (inset).

as-deposited case, demonstrating the stability of this interface. There is a slight shift in relative energy after the 400 °C anneal, while after 500 °C, there is a more pronounced shift of 0.20 eV from as deposited. This reduction in energy separation of the core levels directly indicates a reduction in valence-band offset of the same value. Additionally, after the 500 °C anneal, a clear feature emerges at ∼3 eV higher binding energy than the main Ge 3*d* core lines, which is ascribed to oxidized Ge, i.e., GeO_x formation at the interface. This behavior is notably opposite to HfO_2 films, which have been observed to get oxygen from the native GeO_x upon annealing [49].

We also measured the high-frequency capacitance-voltage characteristics at 100 kHz of am-Al_2O_3/p-Ge MOS capacitors for as-deposited and annealed gate stacks. Figure 5 shows the normalized *C*-*V* curve for both as-deposited and after annealing at 500 °C. All MOS structures showed a fixed positive charge density at the interface. This is evident from

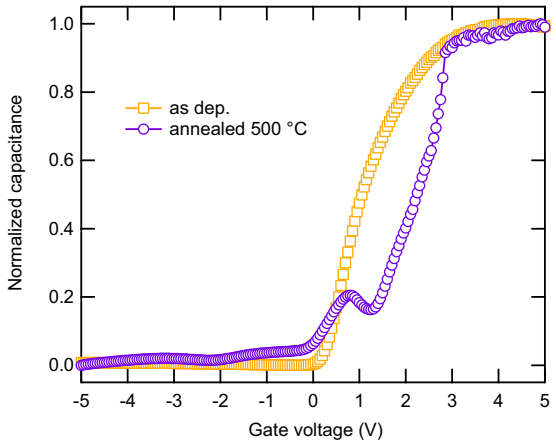

FIG. 5. Capacitance-voltage characteristics of Al/am-Al_2O_3/Ge MOS structures before and after annealing to 500 °C measured at a frequency of 100 kHz.

the sharp up-turn in the C-V, usually referred to as the flat-band voltage. However, only the 500 °C annealed stack shows a marked shift to a more positive flat-band voltage as well as an additional bump indicating accumulation of new interface charge. A similar C-V curve was reported for annealed HfO_2/Ge and is related to interfacial $HfGeO_x$ formation [50]. This is consistent with our observation of interfacial GeO_x formation upon annealing above 400 °C.

In summary, we have investigated the energy-band offsets for ALD-grown amorphous Al_2O_3 on clean p-Ge(100) by combining high-resolution HAXPES spectra with appropriate DOS calculations. The am-Al_2O_3 DOS, predicted from a simple weighted average of DOS results for an ensemble of crystalline Al_2O_3 structures, is used to more accurately identify the valence-band maximum than a simple linear fit to the experimental data. A valence-band offset of 2.60 ± 0.1 eV is found for this heterojunction. The measured band offsets as well as capacitance behavior of as-deposited films are robust at least up to 300 °C. Upon annealing at 500 °C, a GeO_x interfacial layer forms and the C-V characteristics of the stack change dramatically. This occurs with a concomitant reduction of the valence-band offset by 0.20 eV.

This combined experimental and theoretical approach, which takes into account the significant band tailing of the amorphous material in addition to experimental resolution and photoionization cross-section effects, results in considerably higher accuracy than previous reports. We believe this approach to be necessary for the accurate determination of the valence-band maxima and band alignments for amorphous or otherwise disordered oxide materials.

The authors are grateful to Conan Weiland for fruitful discussions. The authors thank Mingzhao Liu and Chang-Yong Nam for assistance with ALD growth. Experiments were performed on the GALAXIES beam line at the SOLEIL Synchrotron, France (Proposal No. 20170393). This research used resources of the Center for Functional Nanomaterials and the National Synchrotron Light Source-II, U.S. Department of Energy Office of Science Facilities, at Brookhaven National Laboratory under Contract No. DE-SC0012704. N.F.Q. acknowledges the financial support of a National Institute of Standards and Technology (NIST) National Research Council (NRC) Research Postdoctoral Associateship Award at the Material Measurement Lab.

Certain commercial software is identified in this paper to adequately describe the methodology used. Such identification does not imply recommendation or endorsement by the National Institute of Standards and Technology, nor does it imply that the software identified is necessarily the best available for the purpose.

[1] S. M. Sze, *Semiconductor Devices, Physics and Technology* (Wiley, Toronto, 1985).
[2] J. Robertson, J. Vac. Sci. Technol. B Microelectron. Nanom. Struct. **18**, 1785 (2000).
[3] L. Weston, H. Tailor, K. Krishnaswamy, L. Bjaalie, and C. G. Van de Walle, Comput. Mater. Sci. **151**, 174 (2018).
[4] E. A. Kraut, R. W. Grant, J. R. Waldrop, and S. P. Kowalczyk, Phys. Rev. Lett. **44**, 1620 (1980).
[5] E. A. Kraut, R. W. Grant, J. R. Waldrop, and S. P. Kowalczyk, Phys. Rev. B **28**, 1965 (1983).
[6] J. C. Woicik, *Hard X-ray Photoelectron Spectroscopy (HAXPES)*, Springer Series in Surface Sciences (Springer, New York, 2015), Chap. 15.
[7] S. Swaminathan, Y. Sun, P. Pianetta, and P. C. McIntyre, J. Appl. Phys. **110**, 094105 (2011).
[8] R. K. Chellappan, D. Rao Gajula, D. McNeill, and G. Hughes, J. Appl. Phys. **114**, 084312 (2013).
[9] M. K. Hudait, Y. Zhu, D. Maurya, S. Priya, P. K. Patra, A. W. Ma, A. Aphale, and I. Macwan, J. Appl. Phys. **113**, 134311 (2013).
[10] X. Wang, J. Xiang, W. Wang, C. Zhao, and J. Zhang, Surf. Sci. **651**, 94 (2016).
[11] M. B. Clavel and M. K. Hudait, IEEE Electron Device Lett. **38**, 1196 (2017).
[12] C. Claeys and E. Simoen, *Germanium-Based Technologies: From Materials to Devices* (Elsevier Science, New York, 2011).
[13] H. S. H. Shang, H. Okorn Schmidt, K. K. Chan, M. Copel, J. A. Ott, P. M. Kozlowski, S. E. Steen, S. A. Cordes, H.-S. P. Wong, E. C. Jones, and W. E. Haensch, in *International Electron Devices Meeting*, Technical Digest (IEEE, 2002), pp. 441–444.
[14] A. K. Rumaiz, T. Krings, D. P. Siddons, A. J. Kuczewski, D. Protic, C. Ross, G. De Geronimo, and Z. Zhong, IEEE Trans. Nucl. Sci. **61**, 3721 (2014).
[15] A. Rumaiz, A. Kuczewski, J. Mead, E. Vernon, D. Pinelli, E. Dooryhee, S. Ghose, T. Caswell, D. Siddons, A. Miceli, J. Baldwin, J. Almer, J. Okasinski, O. Quaranta, R. Woods, T. Krings, and S. Stock, JINST **13**, C04030 (2018).
[16] M. Meuris, A. Delabie, S. Van Elshocht, S. Kubicek, P. Verheyen, B. De Jaeger, J. Van Steenbergen, G. Winderickx, E. Van Moorhem, R. L. Puurunen, B. Brijs, M. Caymax, T. Conard, O. Richard, W. Vandervorst, C. Zhao, S. De Gendt, T. Schram, T. Chiarella, B. Onsia, I. Teerlinck, M. Houssa, P. W. Mertens, G. Raskin, P. Mijlemans, S. Biesemans, and M. M. Heyns, Mater. Sci. Semicond. Process. **8**, 203 (2005).
[17] P. O'Connor and G. De Geronimo, Nucl. Instrum. Methods Phys. Res. Sect. A **480**, 713 (2002).
[18] R. L. Puurunen, J. Appl. Phys **97**, 121301 (2005).
[19] G. Kresse and J. Furthmüller, Phys. Rev. B **54**, 11169 1996).
[20] J. P. Perdew, A. Ruzsinszky, J. Tao, V. N. Staroverov, G. E. Scuseria, and G. I. Csonka, J. Chem. Phys. **123**, 062201 (2005).
[21] P. E. Blöchl, Phys. Rev. B **50**, 17953 (1994).
[22] G. Kresse and D. Joubert, Phys. Rev. B **59**, 1758 (1999).
[23] D. Céolin, J. M. Ablett, D. Prieur, T. Moreno, J. P. Rueff, T. Marchenko, L. Journel, R. Guillemin, B. Pilette, T. Marin, and M. Simon, J. Electron. Spectrosc. Relat. Phenom. **190**, 188 (2013).
[24] J. P. Rueff, J. M. Ablett, D. Céolin, D. Prieur, T. Moreno, V. Balédent, B. Lassalle-Kaiser, J. E. Rault, M. Simon, and A. Shukla, J. Synchrotron Radiat. **22**, 175 (2015).

[25] M. Gaowei, E. M. Muller, A. K. Rumaiz, C. Weiland, E. Cockayne, J. Jordan-Sweet, J. Smedley, and J. C. Woicik, Appl. Phys. Lett. **100**, 201606 (2012).

[26] I. Levin and D. Brandon, J. Am. Ceram. Soc. **81**, 1995 (2005).

[27] K. Nomura, H. Ohta, A. Takagi, T. Kamiya, M. Hirano, and H. Hosono, Nature (London) **432**, 488 (2004).

[28] A. Walsh, J. L. Da Silva, and S. H. Wei, Chem. Mater. **21**, 5119 (2009).

[29] N. F. Mott, Adv. Phys. **26**, 363 (1977).

[30] H. C. Chang, P. S. Yu, T. W. Huang, Y. L. Lin, and F. R. Hsu, in *Proceedings of the Fourth IEEE Symposium on Bioinformatics and Bioengineering* (IEEE, 2004), pp. 293–300.

[31] H. Momida, T. Hamada, Y. Takagi, T. Yamamoto, T. Uda, and T. Ohno, Phys. Rev. B **73**, 054108 (2006).

[32] S. Davis and G. Gutiérrez, J. Phys. Condens. Matter **23**, 495401 (2011).

[33] S. Nahas, A. Gaur, and S. Bhowmick, J. Chem. Phys. **145**, 014106 (2016).

[34] W. W. Tipton and R. G. Hennig, J. Phys. Condens. Matter **25**, 495401 (2013).

[35] B. Revard, W. Tipton, and R. Hennig, *Structure and Stability Prediction of Compounds with Evolutionary Algorithms*, Topics in Current Chemistry Vol. 345 (Springer International, New York, 2014), pp. 181–222.

[36] See Supplemental Material at http://link.aps.org/supplemental/10.1103/PhysRevMaterials.2.114605 for the optimized structures of all 139 (meta)stable Al_2O_3 structures found in VASP-POSCAR format. The files are named POSCAR.N, where N is an integer corresponding to the order in which the structure was optimized in the genetic algorithm run. The file run data give the corresponding VASP calculated energy of each structure in units of eV per atom.

[37] T. D. Veal, N. Feldberg, N. F. Quackenbush, W. M. Linhart, D. O. Scanlon, L. F. J. Piper, and S. M. Durbin, Adv. Energy Mater. **5**, 1501462 (2015).

[38] M. J. Wahila, K. T. Butler, Z. W. Lebens-Higgins, C. H. Hendon, A. S. Nandur, R. E. Treharne, N. F. Quackenbush, S. Sallis, K. Mason, H. Paik, D. G. Schlom, J. C. Woicik, J. Guo, D. A. Arena, B. E. White, G. W. Watson, A. Walsh, and L. F. J. Piper, Chem. Mater. **28**, 4706 (2016).

[39] J. H. Scofield, Lawrence Livermore Laboratory, Report No. UCRL-51326, 1973 (unpublished).

[40] J. C. Woicik, E. J. Nelson, L. Kronik, M. Jain, J. R. Chelikowsky, D. Heskett, L. E. Berman, and G. S. Herman, Phys. Rev. Lett. **89**, 077401 (2002).

[41] H. Momida, S. Nigo, G. Kido, and T. Ohno, Appl. Phys. Lett. **98**, 042102 (2011).

[42] K. Nomura, T. Kamiya, H. Yanagi, E. Ikenaga, K. Yang, K. Kobayashi, M. Hirano, and H. Hosono, Appl. Phys. Lett. **92**, 202117 (2008).

[43] S. Sallis, K. T. Butler, N. F. Quackenbush, D. S. Williams, M. Junda, D. A. Fischer, J. C. Woicik, N. J. Podraza, B. E. White, A. Walsh, and L. F. J. Piper, Appl. Phys. Lett. **104**, 232108 (2014).

[44] S. Sallis, N. F. Quackenbush, D. S. Williams, M. Senger, J. C. Woicik, B. E. White, and L. F. J. Piper, Phys. Status Solidi A **212**, 1471 (2015).

[45] Y. Du, P. V. Sushko, S. R. Spurgeon, M. E. Bowden, J. M. Ablett, T.-L. Lee, N. F. Quackenbush, J. C. Woicik, and S. A. Chambers, Phys. Rev. Mater. **2**, 094602 (2018).

[46] D. Colleoni, G. Miceli, and A. Pasquarello, Appl. Phys. Lett. **107**, 211601 (2015).

[47] S. Miyazaki, J. Vac. Sci. Technol. B Microelectron. Nanom. Struct. **19**, 2212 (2001).

[48] V. V. Afanas'ev, M. Houssa, A. Stesmans, C. Merckling, T. Schram, and J. A. Kittl, Appl. Phys. Lett. **99**, 072103 (2011).

[49] P. S. Lysaght, J. C. Woicik, J. Huang, J. Oh, B. G. Min, and P. D. Kirsch, J. Appl. Phys. **110**, 084107 (2011).

[50] S. Van Elshocht, M. Caymax, T. Conard, S. De Gendt, I. Hoflijk, M. Houssa, B. De Jaeger, J. Van Steenbergen, M. Heyns, and M. Meuris, Appl. Phys. Lett. **88**, 141904 (2006).